RSC Advances

PAPER

View Article Online
View Journal | View Issue

Cite this: *RSC Adv.*, 2025, **15**, 16879

Causonis trifolia-based green synthesis of multifunctional silver nanoparticles for dual sensing of mercury and ferric ions, photocatalysis, and biomedical applications†

Zoya Khalid,[a] Akbar Ali,[*b] Abu Bakar Siddique,[*a] Yasir Zaman,[c] Muhammad Faisal Sibtain,[a] Azhar Abbas,[ad] Mohammad Mahtab Alam[e] and Maher S. Alwethaynani[f]

Health and environmental concerns are often raised by the development of antibiotic resistance and water contamination from various aquatic contaminants, including antibiotic residues, dyes, and heavy metal ions. This paper outlines a facile, affordable, and eco-friendly way to address these issues by green synthesis of silver nanoparticles (CT@AgNPs) under sunlight irradiation using *Causonis trifolia* leaf extract (CTLE), known for its medicinal properties. The greenly synthesized CT@AgNPs exhibited antioxidant, antibacterial, and photocatalytic properties and were an effective nanoprobe for the selective detection of Fe^{3+} and Hg^{2+} in water. CT@AgNPs were thoroughly examined using several sophisticated analytical methods, including FTIR, UV-vis spectroscopy, Scanning electron microscopy (SEM), Powder X-ray diffraction (PXRD), Energy dispersive X-ray (EDX), and Zeta potential (ZP). FTIR demonstrated the effective functionalization of CT@AgNPs with the polar leaf extract of *Causonis trifolia*. The optical properties of CT@AgNPs in solution were monitored using UV-vis spectrophotometric analysis. The synthesis of spherical shaped CT@AgNPs with a face-centered cubic geometry and a 12.7 nm average crystallite size was assessed by SEM and XRD, respectively. CT@AgNPs showed a potent antibacterial activity against Gram-positive bacteria (*L. monocytogenes* and *S. epidermidis*) and Gram-negative bacterial strains (*P. aeruginosa* and *B. bronchiseptica*). CT@AgNPs showed high sensitivity for colorimetric detection of Hg^{2+} and Fe^{3+} with a limit of detection of 1.04 μM and 47.57 μM, respectively in spiked water samples, highlighting their potential for use in environmental monitoring applications. CT@AgNPs showed remarkable antioxidant ability, assessed by DPPH, TFC, and TPC assays. On exposure to sunlight, CT@AgNPs also showed good photocatalytic capability by degradation of methyl orange (79%) and crystal violet (77%) with rate constant values of 0.0157 min^{-1}, and 0.0150 min^{-1}, respectively. This work demonstrates the potential of green route-synthesized AgNPs as efficient and sustainable materials for biomedical and environmental applications.

Received 16th March 2025
Accepted 12th May 2025

DOI: 10.1039/d5ra01882j

rsc.li/rsc-advances

1. Introduction

The chaotic environmental pollution due to the misuse of multiple assets is increasing day by day. Technological innovations in industrial fields have made our lives more facile and effortless, but the redundant disposal of waste and industrial effluents has depleted our natural resources.[1] Heavy metal ions are regarded as the most toxic water pollutants as they persist for a longer duration of time in aquatic environments. Chromium, mercury, and lead are considered the most toxic metal ions for human beings due to their carcinogenic nature.[2,3] Since these heavy metal ions are non-biodegradable and carcinogenic, they can cause the death of several aquatic animals by bioaccumulation, damaging the cellular growth and disturbing the homeostasis of cellular ions. Therefore, the strict monitoring and removal of these ions must be ensured in the

[a]*Institute of Chemistry, University of Sargodha, Sargodha 40100, Pakistan*
[b]*Department of Chemistry, Government College University Faisalabad, 38000-Faisalabad, Pakistan. E-mail: akbarali@gcuf.edu.pk; akbarchm@gmail.com; abubakar.siddique@uos.edu.pk; Tel: +92-4839230546*
[c]*Department of Physics, University of Sargodha, Sargodha 40100, Pakistan*
[d]*Department of Chemistry, Government Ambala Muslim College, Sargodha 40100, Pakistan*
[e]*Department of Basic Medical Sciences, College of Applied Medical Science, King Khalid University, Abha 61421, Saudi Arabia*
[f]*Department of Clinical Laboratory Sciences, College of Applied Medical Sciences, Shaqra University, Alquwayiyah, Riyadh, Saudi Arabia*

† Electronic supplementary information (ESI) available. See DOI: https://doi.org/10.1039/d5ra01882j

drinking water reservoirs.[4] Additionally, the disruption of the food chain caused by the death of aquatic animals may also damage the ecological balance.[5,6] Among the toxic heavy metal ions, mercury and ferric ions are considered potential hazards in water with the maximum permissible limits of 2 ppb,[7] and 0.3 ppm,[8] respectively. Mercury ions present in drinking water can affect the kidneys, gastrointestinal tract, and even cause neurological disorders, which may lead to memory loss and tremors.[7] While the excess intake of ferric ions can damage cell functioning, produce free radicals, and affect the stomach, liver, and heart functions.[9]

Various analytical techniques, like X-ray fluorescence spectroscopy, gas chromatography, inductively coupled plasma spectroscopy, neutron activation analysis, flame atomic absorption spectroscopy, and energy dispersive X-ray spectroscopy are being employed to detect and estimate the heavy metal ions in water resources.[10,11] These methods are regarded as futile due to the high cost and requirement of trained staff for analysis. Therefore, alternative solutions are needed to assess the trace levels of heavy metal ions in water reservoirs.[12] One of the suitable approaches is the use of plasmonic metal NPs based colorimetric sensors. These colorimetric sensors have high sensitivity and can detect water pollutants rapidly. AgNPs are regarded as promising optical sensors that can be used to identify a variety of heavy metal ions and contaminants in water reservoirs. AgNPs having a suitable size, shape, and capped surface can readily detect specific heavy metal ions by interactions based on a redox reaction or aggregation.[13]

Nanotechnology has diversified its applications in several fields. It has employed innovative technology and the synthesis of nano-sized materials at the level of one billionth of a meter. It has overcome the obstacles and hurdles that exist in the path of industrial development.[14,15] Biocompatibility, solid adsorption, and high electron energy are the expedient properties of nanoparticles that help them to sense heavy metal ions in water channels.[16,17]

Nanoparticles have been synthesized using several chemical and physical methods. High cost, release of toxic by-products, and use of toxic precursors are the major drawbacks of these methods. Therefore, biological agents were employed to provide an alternative and a sustainable route.[18] Biogenic synthesis is more advantageous owing to the release of non-toxic by-products and low-cost expenditure.[19] It is a novel method to synthesize nanoscale particles without the addition of external toxic chemicals that cause potential human health problems.[20] One of the phytochemical enriched plant, that has been scarcely used for NPs synthesis is *Causonis trifolia* (*L.*), typically known as fox grape. It is an ethnomedicinally significant twining herb belonging to the Vitaceae family, utilized by several ethnic tribes for its extensive therapeutic benefits. It is enriched with various phytochemical constituents such as flavonoids, nimbidin, saponins, squalene, anthocyanins, myricetin, and tannins, endorsing the plant for a future bioprospecting program as a potential drug option with several biological applications, such as antibacterial, antidiabetic, and antioxidant activities[21,22]

Plant-based biogenic synthesis of NPs is considered as gold standard among other biological methods as it is less toxic and easy to use.[23] The biogenic synthesized AgNPs have specific shapes, sizes, and functional groups on their surface that can impart them specific properties to detect and remediate the pollutants. Therefore, AgNPs have been greenly synthesized for the colorimetric sensing of mercury and ferric ions in water reservoirs.[1]

An important contributing factor to the lack of safe drinking water is the improper disposal of organic dyes in water reservoirs. AgNPs have been previously reported as effective photocatalysts to degrade the hazardous azo dyes before mixing of industrial effluents with freshwater, within a short interval of time.[24] Due to the easy generation of excitons and the ultimate generation of reactive oxygen species (ROS) under sunlight, the AgNPs can easily degrade organic pollutants by redox reactions.[25] Hence, the greenly synthesized AgNPs have also been evaluated for photocatalytic applications.

Bacterial infections are among major concerns that are leading cause of death of animals and human beings in recent years. The pathogenic resistance against antibiotics is increasing day by day.[26] The main factors contributing to the rise in multidrug-resistant bacterial strains are mutation and overuse of medications.[27] AgNPs have been used as alternative antibiotic agents as they are highly toxic to microorganisms.[28] They penetrate the cell membrane of bacterial strains and accumulate in the cytoplasm, where ROS are generated. It helps to inhibit the synthesis of bacterial DNA, mRNA, and proteins, along with the disruption of mitochondria and the electron transport chain, eventually leading to the death of bacterial strains.[29]

In this work, AgNPs were synthesized using the leaf extract of *Causonis trifolia via* the green synthesis method. This plant has therapeutic importance as it is used to cure scurvy, diabetes, tumors, and its roots are utilized as antidotes to snake venom.[21] Powder XRD, FTIR, SEM, EDX, and UV-visible spectroscopy were used to characterize these NPs. The phytochemical constituents in the leaf extract of *Causonis trifolia* acted as reducing and stabilizing agents. AgNPs were synthesized under sunlight exposure for a couple of minutes. These synthesized AgNPs were used as antibacterial agents, antioxidant agents, photocatalysts, and colorimetric sensors for mercury and ferric ions detection in actual water samples.

2. Experimental

2.1. Materials and methods

The leaves of *Causonis trifolia* were collected from Phalia tehsil, district Mandi Bahauddin, Punjab, Pakistan. All the details of chemicals and instruments used has been mentioned in under heading S1 of ESI.†

2.2. Preparation of CTLE

CTLE was prepared by following the already reported procedure in our previous studies.[30] Briefly, the leaves of *Causonis trifolia* were collected from the local nursery of Sargodha, Pakistan. These leaves were washed twice with distilled water (DW) to remove the dust, followed by drying in the shade for 15 days.

These dried leaves were finely ground and filtered through 75 μm mesh size sieves. A fine sieve with a 75 μm mesh size was used to filter the dry leaves after they had been crushed. 2.5 g of the fine leaf powder was mixed with 50 mL of distilled water in a round-bottom flask, and the mixture was refluxed at 80 °C for 2 hours. After filtration by Whatman paper no. 42, the filtrate was stored in a refrigerator for later use.

2.3. Synthesis of CTLE-mediated AgNPs

Freshly prepared CTLE solution (10 mL) was mixed with a 10 mM solution of $AgNO_3$ (85 mg/50 mL of DW). The solution turned from colorless to brownish after exposure to sunlight for 3 minutes, indicating the synthesis of CT@AgNPs. Subsequently, CT@AgNPs were obtained by centrifuging the mixture at 6000 rpm for 30 minutes. To get rid of any unreacted material, these AgNPs were washed three times with distilled water. Following synthesis, CT@AgNPs were dried for 24 hours at 45 °C and stored for further use. General scheme of synthesis of CT@AgNPs is presented in Fig. 1.

2.4. Antibacterial assay

The antibacterial efficacy of CT@AgNPs was evaluated using the agar well diffusion assay.[31] To cultivate the bacterial strains, Mueller–Hinton (MH) agar medium was made by mixing 4 g of agar in 100 mL of DW. The solution was autoclaved. Each Petri dish beneath the laminar flow cabinet was filled with 25 mL of the solution. The bacterial strains were introduced to labelled Petri plates. For *P. aeruginosa*, *B. bronchiseptica*, and *L. monocytogenes* bacterial strains, the identical protocol was followed. Following bacterial sticking, five wells measuring 6 mm in diameter were carved out of the nutritional agar using a sterile cork borer. A suspension solution containing 40 μL of CT@AgNPs in DW (5 mg per mL) was introduced into each well. DW was employed as negative control. These Petri dishes were then incubated for 24 h at 37 °C. The diameter of the inhibitory zones (mm) was used to measure the antibacterial impact of CT@AgNPs on each bacterial strain.

2.5. Colorimetric sensing of heavy metal ions using CT@AgNPs

The capacity of CT@AgNPs to selectively sense hazardous heavy metal ions, such as Pb(II), Fe(II), Cd(II), Fe(III), Hg(II), Na(I), Co(II), Cu(II) and Ni(II) ions in spiked water was investigated using colorimetric sensing probes.[32,33] This was accomplished by mixing 2 mL (1 mM) solution of these heavy metal ions into the CT@AgNPs suspension (2 mg/5 mL). When 2 mL of Fe^{3+} and Hg^{2+} solutions were introduced to 2 mL suspension of CT@AgNPs, there was a noticeable color shift from brownish to colorless. Conversely, the addition of other heavy metal ion solutions under study did not signify any discernible alteration in the brownish color of the solution. The UV-Vis spectrum of as-synthesized CT@AgNPs revealed a noticeable shift and decrease in their localized surface plasmon resonance (LSPR) peak following interaction with Hg^{2+} and Fe^{3+} ions, supporting this observation. This alteration was ascribed to Ag^0 oxidizing to Ag^+.

2.6. Photocatalytic activity of CT@AgNPs

The photocatalytic capability of the catalyst was tested for the degradation of crystal violet (CV) and methyl orange (MO) dyes, following the literaure.[34,35] These dyes were selected due to their widespread use, easy availability, and presence in the wastewater of textile industries. Moreover, MO is anionic and CV is cationic, hence, the potential of CT@AgNPs against all types of

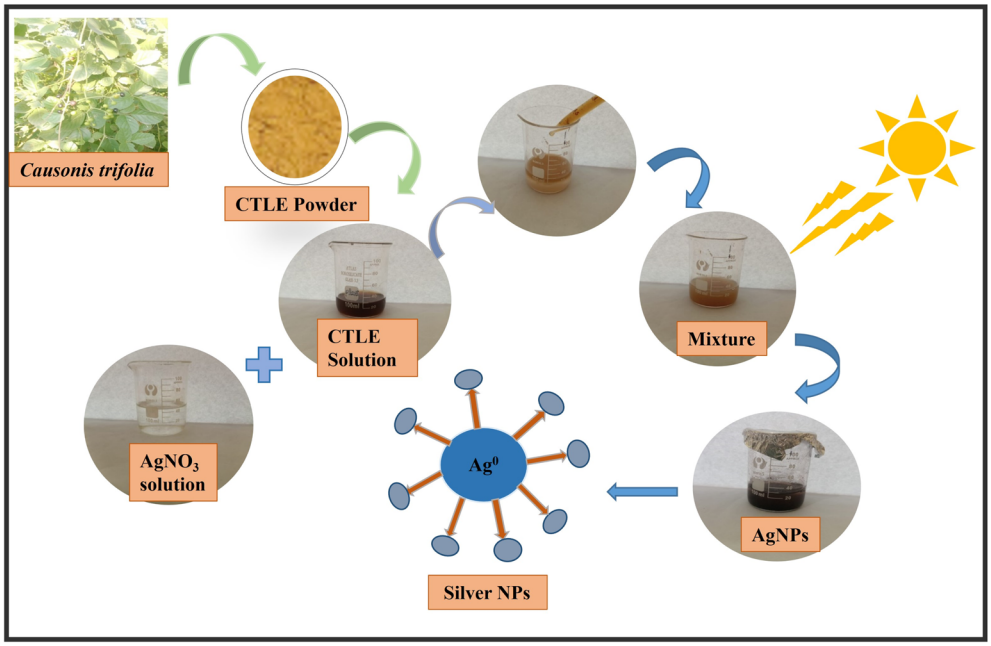

Fig. 1 Schematic representation of CTLE and the biogenic synthesis of CT@AgNPs.

azo dyes can be evaluated. The photocatalytic degradation of MO and CV was performed following the reported procedure. Briefly, the 10 ppm solutions of dyes were prepared by dissolving 5 mg of these dyes in 500 mL of DW. To establish adsorption–desorption equilibria, 20 mg of CT@AgNPs were stirred in 20 mL of the dyes' solutions and keptthe the flasks in the dark for 30 minutes. The reaction flasks were then placed in direct sunshine, and the absorbance of the solutions was measured every 10 minutes for 100 minutes. The absorbance value steadily dropped while the solution's hue drastically faded. The efficiency rate was calculated using eqn (1).

$$\text{Degradation}(\%) = \frac{A_0 - A}{A_0} \times 100 = \frac{C_0 - C}{C_0} \times 100 \quad (1)$$

where C_0, A_0 indicated the concentration and absorbance of dye at initial conditions, and the concentration and C and A indicated the concentration and absorbance of dye at specific time interval of 't', respectively.

2.7. Antioxidant assay

2.7.1. DPPH scavenging activity. DPPH functions as a stable free radical that interacts chemically with the sample's hydrogen or electrons. As a result of this reaction, a diphenyl picrylhydrazine molecule is produced, which causes a prominent color shift from purple to yellow and shows the antioxidant potential of the sample molecules.[36] Green-synthesized CT@AgNPs in varying concentrations of 100 to 500 μg mL^{-1} were dissolved in 3 mL of an ethanolic DPPH solution (4 mg/100 mL), following the addition of ethanol (99.8%) to each sample to make the final volume up to 10 mL. The absorbance of ascorbic acid (reference solution) and test sample was taken at 517 nm after incubation at room temperature for 30 minutes in dark. The following formula (eqn (2)) was used to calculate the percentage scavenging activity of (DPPH) antioxidant activity:

$$\text{Radical scavenging activity}(\%) = \frac{(A_{C517} - A_{S517})}{A_{C517}} \times 100 \quad (2)$$

'A_{C517}' and 'A_{S517}' represent the absorbance value of the control and sample at 517 nm wavelength, respectively.

2.7.2. Total phenolic content (TPC) assay. The total phenolic content of CT@AgNPs was measured following the Folin–Ciocalteu test.[37] A standard curve with gallic acid (GA) was established using the relation of absorbance-concentration. A 2 mL DH_2O solution was first added to 250 μL of 1 N Folin Ciocalteu's phenol solution, followed by varying concentrations of CT@AgNPs (100–500 μL; 1 mg mL^{-1}). The final blend was then allowed to sit at room temperature in dark for 8 minutes. Further, 950 μL of DH_2O and 750 μL of 20% Na_2CO_3 solution were added to each sample. After incubation of 30 min in the dark, the absorbance of each solution was recorded at 765 nm. The results of the greenly synthesized CT@AgNPs sample were reported as (μg (GAE μg mL^{-1})).

2.7.3. Total flavonoid content (TFC) assay. TFC value of sample was measured following the reported literature.[37] The varying concentrations of CT@AgNPs (100 to 500 μL; 1 mg mL^{-1}) were combined with 0.75 mL of methanol, and the volume of the resulting solution was raised to 2 mL by adding distilled H_2O. The samples were then incubated for 10 minutes at 37 °C after adding 300 μL of 10% $AlCl_3$ solution and 5% $NaNO_3$ solution to each sample, as reported in previous literature, with a few changes. The volume of each solution was then increased to 5 mL by adding 2 mL of NaOH solution (1 mol L^{-1}) and DH_2O. After 40 minutes of incubation at room temperature, the absorbance of each solution was measured at 510 nm.

2.8. Statistical analysis

Each experiment was performed thrice, and average results were reported along with the standard deviation values. Statistical significance of results was assessed by ANOVA with threshold value of $p < 0.05$.

3. Results and discussions

3.1. Characterization of CT@AgNPs

The exposure of $AgNO_3$ solution to sunlight generates hydrated electrons within the system. These electrons facilitate the reduction of monovalent silver cations to zero-valent silver atoms.[38] In the current investigation, the biogenic synthesis of AgNPs was carried out using polar extract of *Causonis trifolia* as a reducing agent in sunlight. A noticeable color shift from colorless to red brown in the reaction media was noted due to reduction of Ag^+ to Ag^0, signifying the synthesis of AgNPs.

3.2. UV-vis spectral analysis

CT@AgNPs were synthesized by mixing CTLE and $AgNO_3$ solution and exposing the mixture to sunlight. The effect of exposure time indicated that the optimized CT@AgNPs were prepared on an exposure time of 3 min, as shown in Fig. S1.† The exposure time of the mixture greater or less than 3 min indicated the broadening and shifting of localized surface plasmon resonance peak (LSPR), as depicted in Fig. S1.† The absorption peaks' red shift, which occurs simultaneously with band broadening, showed that CTLE@AgNPs are gradually nucleating and growing, generating comparatively bigger particles over time. UV-visible spectra of CTLE and optimized CT@AgNPs suspension (Fig. 3a) were compared to verify the successful synthesis of CT@AgNPs. The emergence of a noticeable brown color and LSPR peak at 425 nm suggested the formation of AgNPs (Fig. 2a). This outcome is consistent with earlier findings on capped AgNPs.[39] The $AgNO_3$ and CTLE mixture was exposed to sunlight for 3 minutes. After 3 min of sunlight exposure, the UV-vis spectrum showed a distinguishing peak centered at 425 nm, which corresponds to the localized surface plasmon resonance (LSPR) of CT@AgNPs. With the increase in exposure time, λ_{max} were recorded at 435, 443, and 450 nm after 6, 7 and 10 min of exposure, respectively as shown in Fig. S1.† This red shift of the absorption peaks, which occurs simultaneously with a rise in absorption, shows that CT@AgNPs are gradually nucleating and growing, generating comparatively bigger particles with time. This red shift in the distinctive AgNPs peak and band broadening in the absorbance spectra indicated the gradual reduction of Ag^+ to Ag^0, following

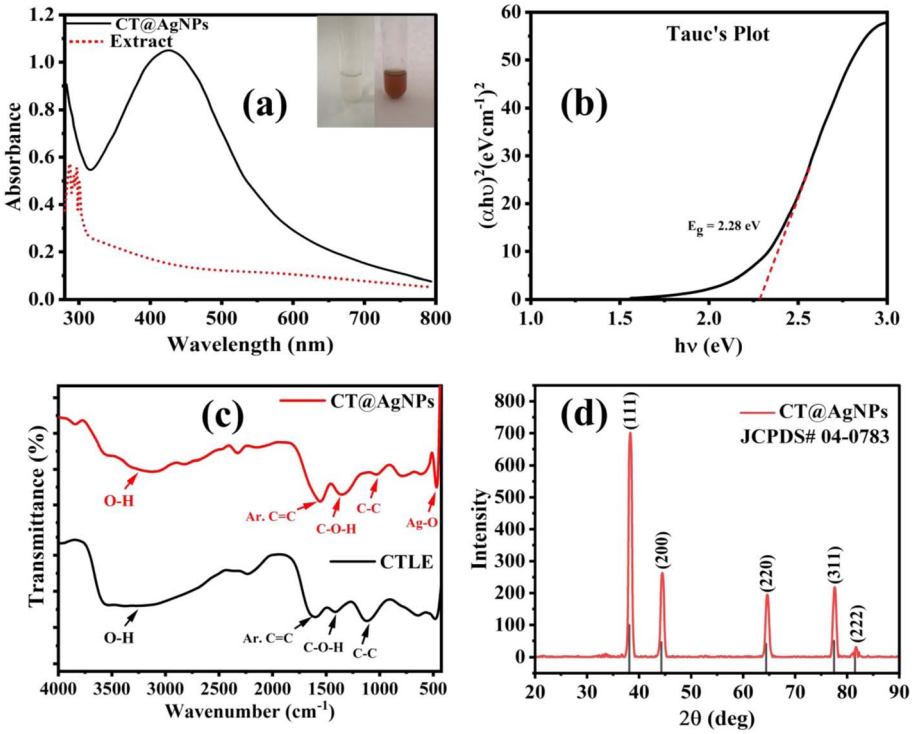

Fig. 2 (a) UV vis. spectrum of CT@AgNPs indicated by solid line and UV vis. Spectrum of *Causonis trifolia* extract indicated by dotted line, (b) band gap energy calculaions of CT@AgNPs using Tauc plot, (c) FTIR spectra of pure leave extract CTLE (black line) and CT@AgNPs (red line), respectively, and (d) PXRD analysis of greenly synthesized CT@AgNPs.

the particle growth with increased AgNPs size.[40] The band gap energy (E_g) of CT@AgNPs was computed using Tauc's equation (eqn (3)):

$$(\alpha h\nu)^{1/n} = B(h\nu - E_g) \quad (3)$$

where 'α' stands for the coefficient of molar extinction, 'h' represents Planck's constant, 'ν' is the frequency, 'B' is a proportional constant, n represents the nature of the electron transition, and its value is $\frac{1}{2}$ for direct energy bandgap (E_g).[36] The E_g value of CT@AgNPs was calculated to be 2.28 eV (Fig. 2b), which is found consistent with the earlier findings in previous literature.[41] The photocatalytic effectiveness of this material is enhanced by its comparatively modest band gap energy, which makes it simple to separate electron–hole pairs when exposed to sunlight.

3.3. FTIR spectra

FTIR spectroscopy was performed to confirm the presence of functional groups in the CTLE and present on the surface of the greenly synthesized CT@AgNPs. FTIR spectra of CTLE and CT@AgNPs (Fig. 2c) confirmed the presence of hydroxyl groups (3200–3400 cm^{-1}), C–C (1326 cm^{-1}), C–O bonds (1030 cm^{-1}), and distinctive Ag–O bond (615 cm^{-1}), reflecting the synthesis of AgNPs with capping of functional groups from CTLE.[42]

3.4. PXRD analysis

PXRD analysis is an important tool to confirm the synthesis, lattice structure, and crystallite properties of metal NPs.[43,44] The average crystallite size and structure of CT@AgNPs were determined using PXRD analysis (Fig. 2d). A series of strong Bragg's reflections with 2θ values of 38.3°, 44.4°, 64.6°, 77.6°, and 81.7° corresponded to lattice planes of (111), (200), (220), (311), and (222), respectively compared with the JCPDS File No. 04-0783. These results were in accordance with the previously reported AgNPs.[45] The Debye–Scherer formula (eqn (4)) was used to calculate the average crystallite size of greenly synthesized CT@AgNPs.

$$D = \frac{K\lambda}{\beta\cos\theta} \quad (4)$$

where, 'D' denotes the average crystallite size of CT@AgNPs, 'K' stands for Scherer constant with value of 0.94 for cubic geometry, 'λ' is the wavelength of X-rays used (0.154 nm), 'β' represents the radian value of peak full width at half maximum (FWHM), and 'θ' is the value of diffraction angle. The average crystallite size of CT@AgNPs was determined to be 12.7 nm using the strong diffracted 2θ value of 38.3° (Table 1). Generally, the surface of NPs increases with the decrease of crystallite size, resulting in better catalytic properties.[46] This small crystallite size (12.73 nm), along with the intermediate crystallinity value (63.62%), demonstrated the high surface area of the CT@AgNPs. The dislocation density of the NPs is an indication of the number of dislocations per unit area, which ultimately

Table 1 Crystallite parameter of CT@AgNPs

Sample	Crystallite size (nm)	Dislocation density $\delta \times 10^{-3}$ (nm^{-2})	Micro strain $\varepsilon \times 10^{-3}$	Crystallinity %
CT@AgNPs	12.73	6.19	1.11	63.62

affects the magnetic and optical properties of the material.[47] Therefore, the value of dislocation density is an important parameter to indicate the different optical properties of the reported CT@AgNPs from the already reported AgNPs. Moreover, the value of microstrain of CT@AgNPs also gave information about the line defects and lattice distortions, which affect the photocatalytic applications of NPs.[48] The values of dislocation density (6.19×10^{-3}) and microstrain (1.11×10^{-3}) indicated modifications in the material's optical properties and surface defects.

3.5. SEM, EDX and ZP analyses

SEM-EDX analyses were performed to determine the surface shape, average particle size, and chemical composition of CT@AgNPs.[49] Fig. 3a demonstrated a spheroidal morphology of CT@AgNPs with an average particle size of 19.2 nm, as illustrated in Fig. S2.† These results were in accordance with previously reported AgNPs.[50] Additionally, EDX was employed to confirm the composition of CT@AgNPs. Fig. 3b illustrates the EDX spectrum of CT@AgNPs.[51] EDX spectrum showed the purity of CT@AgNPs with the prominent peak of Ag at 2.97 keV. Some secondary peaks of carbon and oxygen were also observed in the spectrum at 0.28 keV and 0.55 keV, respectively. These peaks were observed due to the capping of the extract on the AgNPs surface.

The colloidal stability studies of CT@AgNPs conducted by ZP measurements showed the good stability of CT@AgNPs in suspended form in water with a ZP value of -37.1 ± 5.9 mV, as depicted in Fig. 3c. Generally, the value of ZP greater than 30 mV depicts the high stability of NPs in the suspension.[52] This value demonstrates the high electrostatic stability of CT@AgNPs with the negative charge on the surface. A negatively charged surface is generally observed due to the capping of polarizable species on the AgNPs.

3.6. Selective colorimetric sensing of Hg^{2+} and Fe^{3+} using CT@AgNPs

Currently, many functionalized NPs are extensively used as colorimetric sensors for the detection of heavy metal ions in water samples.[53] The sensory potential of CT@AgNPs was evaluated using 1 mM solutions of Hg^{2+}, Fe^{2+}, Fe^{3+}, Ni^{2+}, Cu^{2+}, Na^{+}, Cd^{2+}, Co^{2+}, and Pb^{2+} ions. The addition of Fe^{2+}, Na^{+}, Ni^{2+}, Cu^{2+}, Co^{2+}, Cd^{2+}, and Pb^{2+} solutions did not change the color or UV-vis. Spectra of greenly-synthesized CT@AgNPs suspension. The introduction of Hg^{2+} and Fe^{3+} to CT@AgNPs resulted complete quenching of absorbance of UV-vis spectra of AgNPs

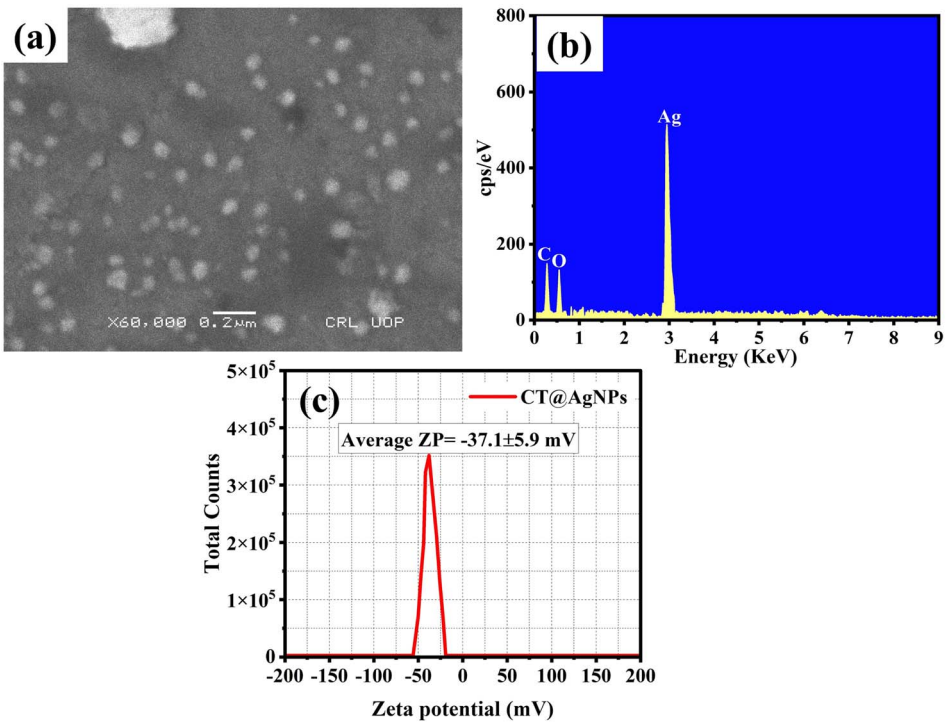

Fig. 3 (a) SEM image of CT@AgNPs, (b) EDX analysis of CT@AgNPs, (c) ZP analysis of CT@AgNPs.

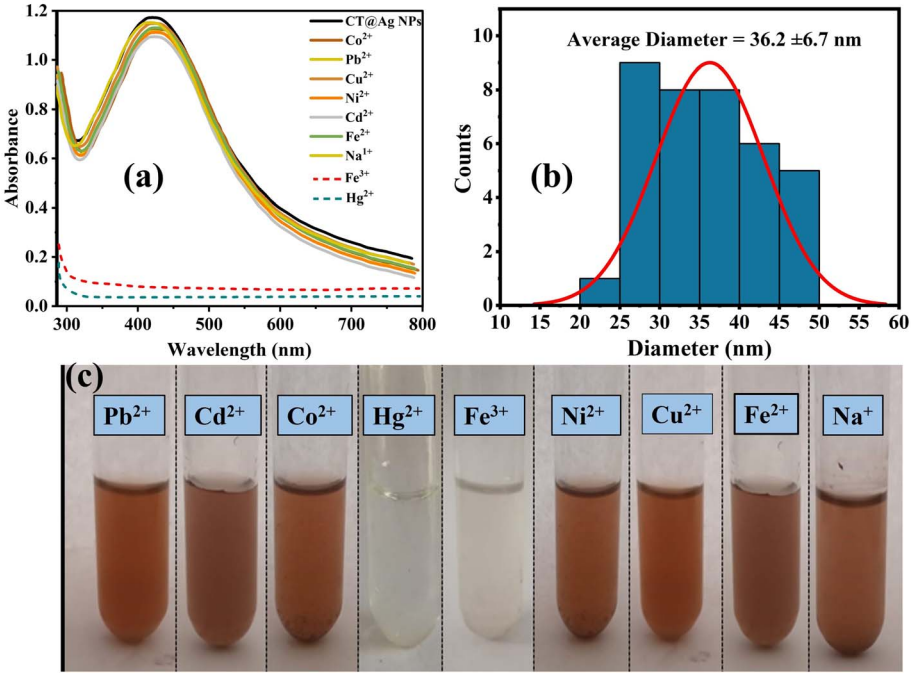

Fig. 4 (a) UV-vis spectra of CT@AgNPs along with various heavy metal ions, (b) bar graph for change in absorbance, and (c) photographic illustration of interaction of CT@AgNPs with different heavy metal ions.

as illustrated in Fig. 4a and b. When added to the CT@AgNPs suspension, Hg^{2+} and Fe^{3+} caused a noticeable, sudden color change from yellowish-brown to colorless, as shown in Fig. 4c. Since Ag and Hg^{2+}, Fe^{3+} ions have unique redox reactions, the presence of other competing ions did not affect the selectivity toward Hg^{2+} and Fe^{3+} ions. This sudden color change in CT@AgNPs and complete quenching of the absorbance of AgNPs by the addition of Hg^{2+} and Fe^{3+} ions to AgNPs suspension made the basis of CT@AgNPs use in selective sensing of these heavy metal ions. The detection of metal ions using AgNPs may be backed up by three primary mechanisms: (i) redox reaction,[54] (ii) aggregation and complexation route,[5] (iii) Ag–Hg alloy formation.[55] In the aggregation mechanism, metal ions and AgNPs combine to create a stable complex *via* their capping agent, which causes the NPs to aggregate. This aggregation causes a significant red shift in λ_{max} of the AgNPs on interaction with a specific heavy metal ion. The type of metal ion interaction depends upon the reducing and stabilizing agent of the NPs. In redox process, Ag^0 is oxidized to Ag^+ by Hg^{2+} and Fe^{3+} ions, which causes Ag to dissolve and the solution becomes discolored. CT@AgNPs and Hg^{2+}, Fe^{3+} ions undergo a redox reaction, which is primarily responsible for the color change of the suspension upon the addition of these ions. In these redox processes, either there is no shift in λ_{max} or a slight blue shift is observed. In the present study, the sensing of heavy metal ions took place through redox process as there was no shift in λ_{max} was observed. The standard electrochemical redox potentials of Ag, Fe^{3+}, and Hg^{2+} serve as the foundation for this particular redox process. Fe^{2+}/Fe^{3+}, Hg/Hg^{2+} and Ag/Ag^+ have typical redox potentials of +0.77 V, +0.85 V and +0.80 V, respectively.[56–58] As a result, Ag can readily oxidize to Ag^+ while concurrently reducing Hg^{2+} to Hg^0 and Fe^{3+} to Fe^{2+}. Each of these three routes would show a different shift in the peak position, but they would primarily result in a change of the SPR peak intensity and colour change as shown in Fig. 4a and c.

3.6.1. Evaluation of CT@AgNPs to determine the LOD of Hg^{2+} ions. The limit of detection (LOD) of Hg^{2+} is determined by the decrease in characteristic SPR peak intensity of CT@AgNPs UV vis spectra. Using eqn (5)–(7) the value of LOD, limit of quantification (LOQ), and relative change in absorption were determined for the analysis of Hg^{2+} and Fe $^{3+}$ in actual water samples:

$$\mathrm{LOD} = \frac{3\sigma}{S} \tag{5}$$

$$\mathrm{LOQ} = \frac{10\sigma}{S} \tag{6}$$

where 'σ' represents the standard deviation of the intercept and 'S' represents the slope of calibration curve of the response. A confidence level of roughly 99% is guaranteed by factor 3, meaning that the signal can be consistently distinguished from the background noise.

Eqn (6) was used to determine the change in absorption:

$$\text{Relative change in absorbance} = \frac{A_{\mathrm{Control}} - A_{\mathrm{sample}}}{A_{\mathrm{Control}}} \tag{7}$$

where $A_{control}$ is the initial absorbance of CT@AgNPs, and A_{sample} is the absorbance of the CT@AgNPs following the addition of the analyte. The quantitative reduction in amplitude of the LSPR is due to the concentration increase of Hg^{2+}. (Fig. 5a and b) shows a linear calibration curve between the absorbance change $\Delta A = A_{control} - A_{Hg}/A_{control}$ and the dilutions of Hg^{2+} (2–

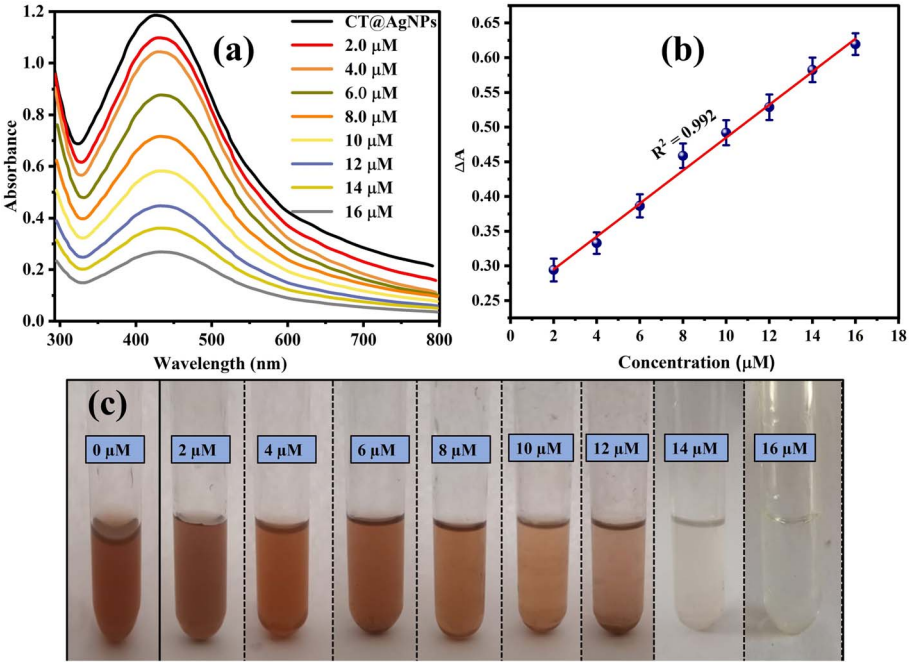

Fig. 5 (a) UV-vis spectra of CT@AgNPs with various dilutions of Hg^{2+} ions, (b) determination of LOD using calibration curve between change in absorbance and concentration, and (c) photographic illustration of colorimetric sensing of Hg^{2+} ions with naked eye using CT@AgNPs.

16 μM) with LOD value of 1.04 μM and $R^2 = 0.992$. The LOQ value was calculated to be 3.12 μM.

3.6.2. Evaluation of CT@AgNPs to determine the LOD of Fe^{3+} ions. The decrease in intensity of SPR peak in the UV-vis spectra of CT@AgNPs as indicated in Fig. 8a demonstrated the selective sensing of Fe^{3+} ions in spiked real water sample using CT@AgNPs. The intensity of the distinctive SPR peak quantitatively reduced as the concentration of Fe^{3+} ions increased. Fig. 6a and b showed a linear relationship between the absorbance change, relative change in absorbance $= A_{control} - A_{Fe}/A_{control}$, and the concentration of Fe^{3+} ions with a dilution range of 100–800 μM, resulting in LOD value of 47.57 μM and LOQ value of 142.71 μM.

3.6.3. Analysis of Hg^{2+} and Fe^{3+} in real water samples. Hg^{2+} and Fe^{3+} detection was performed in real samples of tap water (Research Laboratory at the University of Sargodha) and river water (Jhelum River in the district of Sargodha), as illustrated in Table 2 and Table 3, respectively. The efficacy of CT@AgNPs to detect Hg^{2+} and Fe^{3+} in actual water samples was demonstrated by a recovery rate of over 90% and an RSD value of less than 3%.

In addition to the high recovery rate, the comparison of the LOD values of greenly synthesized AgNPs demonstrated the high sensitivity of CT@AgNPs for heavy metal ions (Hg^{2+} and Fe^{3+}) detection, as illustrated in Table S1.†

3.7. Antibacterial assay

The antibacterial efficacy of CT@AgNPs was evaluated against both Gram-positive pathogens (*L. monocytogenes* and *S. epidermidis*) and Gram-negative bacterial strains (*P. aeruginosa* and *B. bronchiseptica*) using the agar well diffusion method.[14] The inhibition zones of antibacterial activity against these pathogens are illustrated in Fig. 7a and Table 4, notably greater than the negative control (DW). The polar extract of *Causonis trifolia* also showed evident antibacterial results against these bacterial strains. The results of antibacterial activity of CT@AgNPs were comparable to the widely used antibiotic "erythromycin". CT@AgNPs were found to have greater antibacterial efficacy against Gram-positive bacterial strains as compared to Gram-negative bacterial strains (Fig. S3†).

The exact mechanism of action of NPs against bacterial strains is still unknown, however, it has been speculated that the NPs hinder the bacterial growth by: (1) rupturing the cell barriers of bacteria by direct interaction od generation of ROS in the vicinity, (2) generation of ROS inside the cell on entrance, or (3) by inhibiting the normal functioning of DNA and growth proteins by interacting with them. The variation of activity of AgNPs against various bacterial strains is dependent on the shape, size, dose, capping agent of AgNPs, and composition of the cell barriers of bacterial cells.[59] The cell wall of Gram-positive bacteria is made up mainly of peptidoglycan layers, through which NPs can easily pass by interaction with channel proteins, while the cell wall of Gram-negative bacteria is made up of lipopolysaccharide, which is relatively thin but does not allow easy access for NPs to enter the cell. Therefore, the CT@AgNPs were found to be more active against Gram-positive strains than Gram-negative strains. These results were found in concordance to the previously reported activity of greenly synthesized AgNPs.[60] Some NPs are more active against some specific bacterial strains, like the synthesized CT@AgNPs were found more active against *L. monocytogenes* than *S. epidermidis*, which can be ascribed to the better interaction of CT@AgNPs with the glycoproteins of the cell wall of *L. monocytogenes*. *L.*

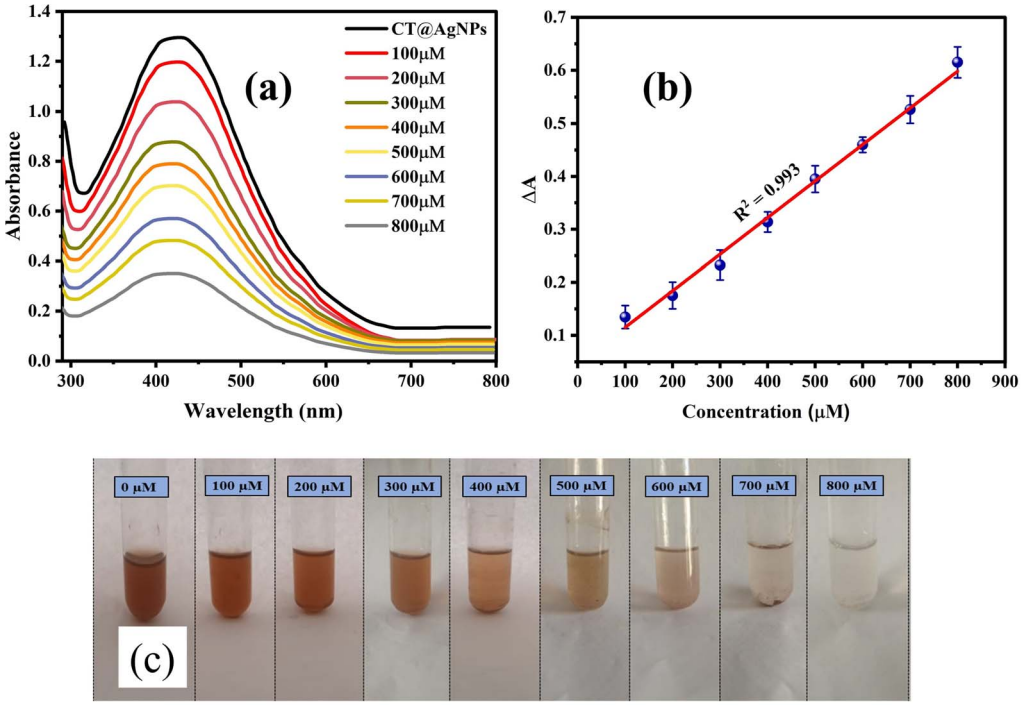

Fig. 6 (a) UV-vis spectra of CT@AgNPs with varying concentrations of Fe^{3+} ions, (b) LOD determination using a calibration curve between change in absorbance and concentration, and (c) colorimetric assay of Fe^{3+} ions with the naked eye using CT@AgNPs.

Table 2 Results for Hg^{2+} detection in river water and tap water samples using CT@AgNPs

Sample	Hg^{2+} added (μM)	Hg^{2+} found (μM)	Recovery (%)	RSD (%) $n = 3$
River water	20	19.48	97.4	1.4
	40	38	95	1.3
	60	58.5	97.5	1.9
Tap water	20	18	90	1.8
	40	36.5	91.25	2.2
	60	56	93.33	2.5

Table 3 Results of Fe^{3+} detection in river water and tap water samples utilizing greenly synthesized CT@AgNPs

Sample	Fe^{3+} added (μM)	Fe^{3+} found (μM)	Recovery (%)	RSD (%) $n = 3$
River water	40	38.5	96.25	0.8
	55	53	96.36	1.5
	70	68	97.14	1.6
Tap water	40	37	92.5	2.1
	55	52.5	95.45	1.9
	70	67.5	96.42	2.3

monocytogenes is more vulnerable to CT@AgNPs attack than *S. epidermidis* because *L. monocytogenes* has a relatively thinner cell wall of average thickness about 20 nm,[61] as compared to the *S. epidermidis* having an average cell wall thickness of 51 nm,[62] that results in the more penetration of CT@AgNPs within the *L. monocytogenes* cell, and more generation of ROS inside the cell, which ultimately causes the cell death.[63] Additionally, the comparison of antibacterial activities of greenly synthesized AgNPs against the tested bacterial strains (Table S2†) also demonstrated the high efficacy of CT@AgNPs to hinder the growth of selected bacterial strains.

3.8. Antioxidant assay

3.8.1. DPPH scavenging activity. DPPH radical scavenging activity is widely used to quantitatively evaluate the antioxidant potential of various compounds. In addition to ascorbic acid, the antioxidant properties of CT@AgNPs were evaluated using a Shimadzu UV-1800 spectrophotometer. The antioxidant results are illustrated in Fig. 7b as the percentage of radical scavenging activity (% RSA). CT@AgNPs had the strongest DPPH free ion scavenging capabilities of 80% at a concentration of 500 μL (1 mg mL^{-1}).[64] CT@AgNPs exhibited greater radical scavenging activity and are nearly identical to ascorbic acid. The metabolically significant compounds that can help to stabilize the NPs include terpenoids, flavonoids, and oxidative anti-stress regulators, according to research.[65]

3.8.2. Total flavonoid content (TFC) assay. A linear calibration curve of the standard (quercetin) yielded the value of intercept $y = 0.0002x$ and $R^2 = 0.9925$. According to the calibration curve equation, the highest total flavonoid content of 70.09 μg QCE μg mL^{-1} was obtained at a 500 μL concentration of CT@AgNPs.[66] This was almost equal to the standard at the same concentration as shown in Fig. 7c.

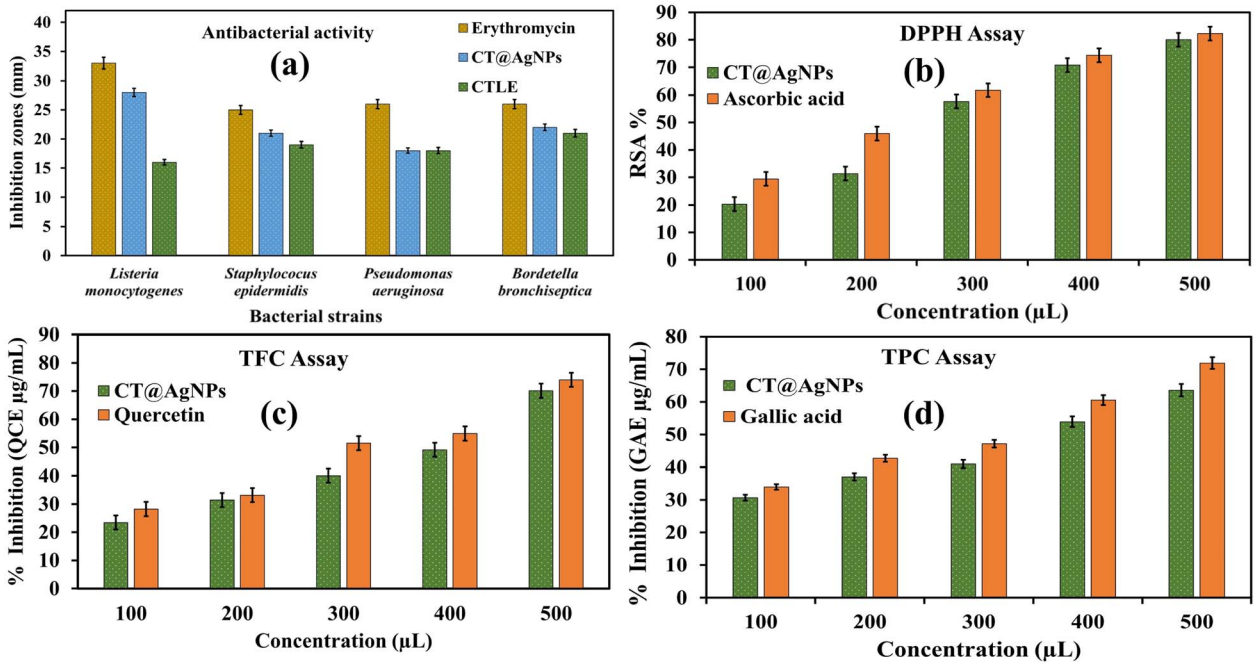

Fig. 7 (a) Bar graph of inhibition zones of CT@AgNPs, standard antibiotic erythromycin, and CTLE, (b) DPPH assay of CT@AgNPs compared with standard antioxidant (ascorbic acid), (c) TFC assay of CT@AgNPs along with quercetin, (d) TPC assay of CT@AgNPs compared with gallic acid.

Table 4 Results of antibacterial activity of erythromycin, CT@AgNPs and CTLE against various bacterial strains

	Zone of inhibition (mm)		
Bacterial strains	Erythromycin	AgNPs	Plant extract
Listeria monocytogenes	33 ± 0.58	28 ± 0.33	16 ± 0.67
Pseudomonas aeruginosa	26 ± 0.58	18 ± 0.33	18 ± 0.88
Staphylococcus epidermidis	25 ± 0.33	21 ± 0.33	19 ± 0.67
Bordetella bronchiseptica	26 ± 0.58	22 ± 0.57	21 ± 0.67

3.8.3. Total phenolic content (TPC) assay. The total phenolic content of greenly synthesized CT@AgNPs was calculated by establishing a linear calibration curve of the standard gallic acid (GA) based on the absorbance and concentration relation. The standard curve with gallic acid yielded the value of intercept $y = 0.0023x$ and R^2 of 0.9808.[67] The phenolic content of CT@AgNPs was (63.5 GAE µg mL^{-1}) at a concentration of 500 µL, according to the calibration curve equation (Fig. 7d).

3.9. Photocatalytic activity for MO and CV dye degradation

3.9.1. Efficiency of photodegradation for MO and CV dyes. Metallic NPs can readily degrade organic dyes due to the facile generation of ROS by absorption of light in the UV or visible region. Therefore, AgNPs with a band gap energy of 2–3 eV can efficiently facilitate the excitation of electrons from the VB to the CB in the near visible region.[68] Greenly synthesized CT@AgNPs were used for the photodegradation of MO and CV dyes under solar irradiation, and it is attributed to its feasible band gap of 2.28 eV and larger surface area. The MO peak at λ_{max} of 464 nm showed a decreasing intensity as the dye faded away gradually, as shown in Fig. 8a. As the exposure time increased, the MO dye concentration steadily decreased reaching its maximum degradation (79%) after 100 minutes, as seen in Fig. 8c and these results were far more better than the previous literature.[69] over time, the intensity of the distinctive peak of CV dye at λ_{max} of 590 nm continued decreasing, as shown in Fig. 8b. As the exposure increased, the concentration of CV dye steadily declined reaching a maximum degradation of 77% after 100 minutes, as illustrated in Fig. 8c, better than previously reported results.[70]

3.9.2. Kinetics of photodegradation for MO and CV dyes. The reaction kinetics of dye degradation were also evaluated to determine the rate constants of reaction.[35] The kinetics of this photocatalytic activity was examined using a graph of $\ln(C_t/C_0)$ *vs.* exposure time (t) (Fig. 8d). According to eqn (8), the photodegradation of MO and CV dyes followed pseudo-1st order reaction kinetics.

$$\ln\frac{C}{C_0} = kt \quad (8)$$

where k denotes the rate constant, C_t and C_0 represent the concentration of dyes at time interval 't' and at zero reaction time, respectively. There was a high level of linearity obtained for both dyes with a regression coefficient value of $R^2 = 0.984$ for MO dye and $R^2 = 0.995$ for CV dye, respectively. The degradation rate constant k is determined by the slope of this linear regression, and for MO dye, a value of $k = 1.57 \times 10^{-2}$ min^{-1} and for CV dye, a value of $k = 1.50 \times 10^{-2}$ min^{-1} was obtained, respectively, as illustrated in Fig. 8d. The comparison of the photocatalytic activity of CT@AgNPs with some previously

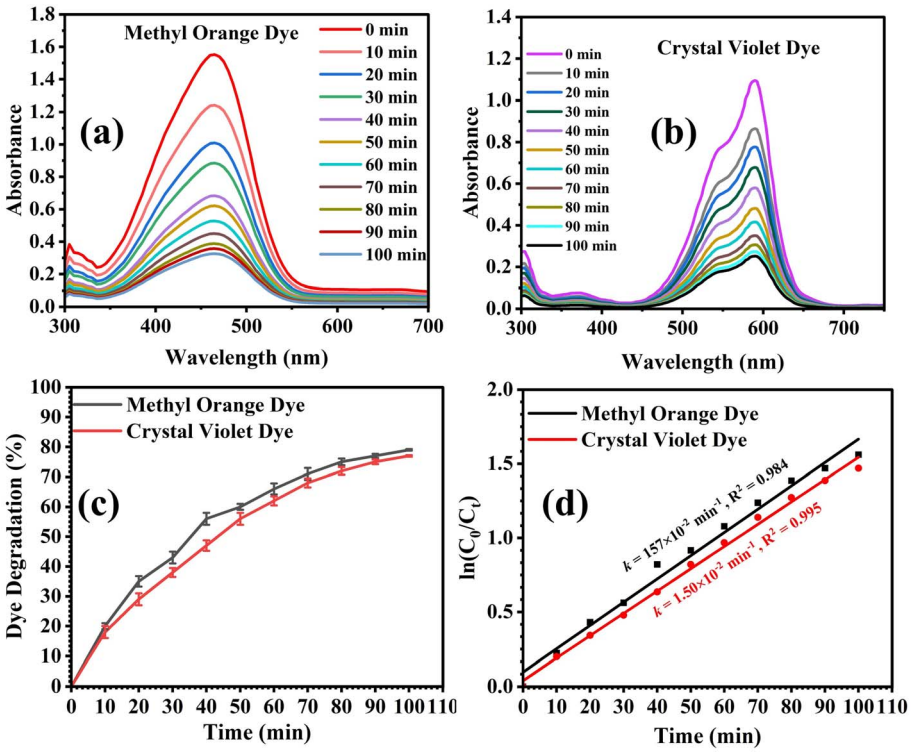

Fig. 8 (a) Absorbance sectrum of methyl orange dye after regular intervals of time, (b) absorbance sectrum of crystal violet dye after regular intervals of time, (c) dye degradation (%) *versus* time graph for methyl orange and crystal violet dyes (d) reaction kinetics plot of degradation of methyl orange and crystal violet dyes.

reported greenly synthesized AgNPs (Table S3†) also showed the efficient nature of CT@AgNPs to degrade azo dyes under sunlight.

3.9.3. Effect of reaction parameters and proposed photocatalytic mechanism for dye degradation. Dye degradation efficiency (%) is affected by several factors, including surface charge, surface area, the extent to which dye is ionized, the number of active sites, and penetration of light in the reaction medium. Batch experiments were conducted to evaluate and optimize the effect of reaction parameters.

The effect of initial dye concentration on the degradation efficiency was evaluated in the concentration range of 10–50 ppm. Degradation was progressively decreased with increased dye concentration due to the increased turbidity, less light penetration in the reaction medium, and decreased adsorption of dye molecules on the NPs surface (Fig. 9a).

By keeping the other conditions same, the effect of catalyst dosage was evaluated in the range of 5–70 mg. It was seen that with increasing the catalyst dose, dye degradation (%) was also increased, and maximum degradation was observed at the catalyst dose of 60 mg, due to the increased number of active sites. But above this concentration (Fig. 9b), the efficiency was decreased slightly, which can be attributed to the less light penetration in the reaction medium and aggregation of NPs.[71]

Adsorption of dye on the catalyst's surface is significantly affected by the pH as it modifies the surface charge and zero-point charge of CT@AgNPs and dye molecules, respectively. The generation of radicals in the reaction medium is also affected by the pH (Fig. 9c) represents the effect of pH in the range of 2 to 12 on the dye degradation efficiency (%). Dye degradation efficiency (%) was increased with the increase in pH, and maximum degradation was observed at pH 8. A further increase in pH resulted in decreased dye degradation.[71]

This might be due to the neutralization of ROS species and decreased adsorption of dye molecules on the NPs surface. Above pH 8, the dye degradation efficiency (%) of the catalyst was decreased due to a decrease in the number of active sites owing to the ionization of the surface of NPs (Fig. 9c). Below pH 8, dye degradation efficiency (%) of the catalyst was decreased successively, which can be attributed to the neutralization of ROS species ($^{\bullet}OH$, $O_2^{\bullet-}$, *etc.*) by H_3O^+ ions at lower pH. Moreover, lower pH caused the NPs to aggregate by lowering their surface charge, resulting in their lowered stability (Fig. 9c).[72]

Radical scavenging experiments were conducted for four scavengers: disodium ethylenediamine acetate (Na_2EDTA) for h^+, *p*-benzoquinone (*p*-BQ) for $O_2^{-\bullet}$, isopropanol (IPA) for $OH^{\bullet}$, and L-ascorbic acid (L-AA) for H_2O_2.[59,71] Findings revealed that dye degradation was decreased in each case which indicates that all ROS were generated reaction medium when exposed to sunlight. Maximum decrease in dye degradation was observed in the case of *p*-BQ and Na_2EDTA, which scavenge $O_2^{-\bullet}$, h^+, respectively. This indicated that $O_2^{-\bullet}$ and h^+ were major ROS species involved in degradation. Relatively minimal decrease in dye degradation was observed in the case of L-AA and IPA, which revealed the minimum participation of H_2O_2 and $OH^{\bullet}$ in the degradation process (Fig. 9d).

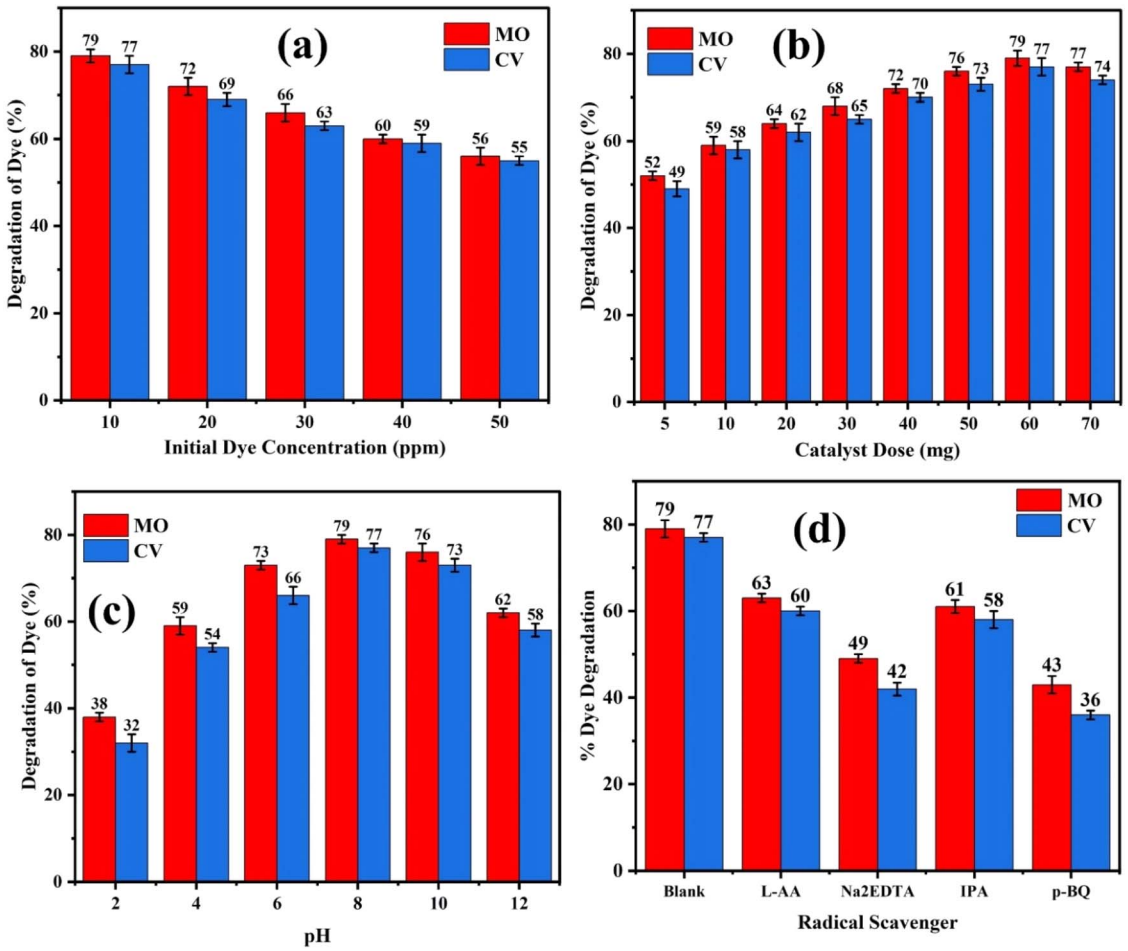

Fig. 9 (a) Effect of dye concentration on degradation efficiency, (b) effect of catalyst dose, (c) effect of pH, (d) effect of radical scavengers on degradation efficiency.

For theoretical insight into the ROS generated in the reaction mixture, Butler–Ginley equations (eqn (9) and (10)) were used to calculate the band edge potentials of the VB and CB required to produce ROS in the system and to link the theoretical results with the experimental data.[35]

$$E_{CB} = X - E_C - 0.5\,E_g \quad (9)$$

$$E_{VB} = E_{CB} + E_g \quad (10)$$

The band edge potential values compared with the normal hydrogen electrode potential are depicted in Fig. S4 in the ESI.† The positions of E_{CB} (−1.21 V) and E_{VB} (+1.08 V) depicted the facile generation $O_2^{-\bullet}$ due to the accessible reduction potential of $O_2/O_2^{-\bullet}$ (−0.33 V). While it was least possible to generate $OH^\bullet$ in the mixture due to inaccessible oxidation potential +2.44 V, required for oxidation of OH^- to $^\bullet OH$. These theoretical results strongly supported the experimental findings of the radical scavenging experiments, as illustrated in Fig. 9. Based on these experiments and previous reported literature,[59] the degradation mechanism of the azo dyes on the CT@AgNPs was proposed as shown by eqn (11)–(19).

$$\text{AgNPs} + h\nu\ (\text{UV-vis}) \rightarrow \text{AgNPs}\ (e^-(\text{CB}) + h^+\ (\text{VB})) \quad (11)$$

$$H_2O\ (\text{ads}) + h^+\ (\text{VB}) \rightarrow OH^\bullet(\text{ads}) + H^+\ (\text{ads}) \quad (12)$$

$$O_2 + e^-\ (\text{CB}) \rightarrow O_2^{\bullet -}\ (\text{ads}) \quad (13)$$

$$O_2^{\bullet -}\ (\text{ads}) + H^+\ (\text{ads}) \rightarrow HOO^\bullet\ (\text{ads}) \quad (14)$$

$$HOO^\bullet\ (\text{ads}) \rightarrow H_2O_2\ (\text{ads}) + O_2 \quad (15)$$

$$H_2O_2\ (\text{ads}) \rightarrow 2OH^\bullet\ (\text{ads}) \quad (16)$$

$$\text{Dye} + 2OH^\bullet + \text{intermediates} \rightarrow CO_2 + H_2O \quad (17)$$

$$\text{Dye} + h^+\ (\text{VB}) \rightarrow \text{oxidation products} \quad (18)$$

$$\text{Dye} + e^-\ (\text{CB}) \rightarrow \text{reduction products} \quad (19)$$

The photocatalytic activity is promoted by efficient separation of photo-generated electrons and prevention of charge carrier recombination. The photodegradation of azo dye molecules can be summarized by the following steps. In the first step, the photocatalyst absorbs the photons of incident visible light to initiate the photocatalytic activity by transfer of

electrons from the VB to the CB, as depicted by eqn (11). In 2nd step, the produced electron–hole pair reacts with the water molecules and dissolved oxygen to generate several ROS by chain reaction, as shown by eqn (12)–(16). In 3rd step, these ROS and excitons react with the dye molecules by redox reactions and cause the degradation, as shown by eqn (17)–(19).[73]

3.9.4. Reusability studies of the photocatalyst. The photocatalytic activity of the synthesized CT@AgNPs catalyst for MO and CV dye was assessed following five consecutive cycles of operation and regeneration to assess its durability and reusability. The greenly synthesized CT@AgNPs catalyst was examined for MO and CV degradation, and it was recovered following each use by centrifuging the reaction mixture for 20 minutes at 6000 rpm. The solid portion of the falcon tube that contained greenly synthesized CT@AgNPs was washed and filtered three times with distilled water. Further, NPs were dried in a Petri dish for four hours at 80 °C in an oven. Afterwards, this dried sample (CT@AgNPs) was evaluated for photocatalytic activity using the same protocol as mentioned above. An already reported recovery process was adapted with few changes.[74] Following five recycling runs, there was a minor drop in the catalyst efficiency (12% for MO dye and 14% for CV dye) was observed as depicted in Fig. S5,† which demonstrated the viability of the CT@AgNPs based catalyst for multi-time applications in wastewater treatment. The metal NPs can be effectively used for wastewater treatment, but the fate and toxicity of these plasmonic NPs due to the leaching of ions remain a concern for the practical applications. The leaching of ions can substantially affect the aquatic ecosystem; therefore, the concentration of leached ions was also assessed by flame atomic absorption spectroscopy (FAAS) in the treated wastewater samples. Since the CT@AgNPs were stable (having a large ZP value) and capped with phytochemicals, there were negligible chances of silver ions leaching. The FFAS analysis showed minimal silver ion release (<0.01 μg L^{-1}) in the treated wastewater. This value is substantially less than the permissible limit of silver ions in drinking water (100 μg L^{-1}). Therefore, it can be concluded that the CT@AgNPs can be used as effective photocatalysts for wastewater treatment applications with minimum implications on the environment.

4. Conclusion

Herein, the green synthesis of CT@AgNPs has been reported using the polar extract of *Causonis trifolia* leaves under sunlight. After characterization of CT@AgNPs through UV-visible and FTIR spectroscopy, PXRD, SEM, EDX, and ZP analysis, the CT@AgNPs have been utilized for the selective sensing of Hg^{2+} and Fe^{3+} ions with LOD values of 1.04 μM and 47.57 μM, respectively. CT@AgNPs were evaluated for the photodegradation of MO and CV dyes in the presence of sunlight, which showed the 79% and 77% degradation efficiency toward MO and CV in just 100 minutes with rate constant values of 1.57 × 10^{-2} min^{-1} and 1.50 × 10^{-2} min^{-1}, respectively. A viable mechanism for degrading these dyes was proposed based on radical scavenging experiments. CT@AgNPs have also shown remarkable antibacterial activities by inhibiting the growth of Gram-positive (*L. monocytogenes* (28 ± 0.33 mm) and *S. epidermidis* (18 ± 0.33 mm)) and Gram-negative (*P. aeruginosa* (21 ± 0.33 mm) and *B. bronchiseptica* (22 ± 0.57 mm)) strains. CT@AgNPs had shown the appreciable DPPH free radical scavenging capability (80%), total flavonoid content of 70.09 μg QCE μg mL^{-1}, and total phenolic content of 63.5 GAE μg mL^{-1}. All these results showed the viability and potential of CT@AgNPs for solutions of environmental and health-related real-world applications at a commercial scale. However, the main limitations that may arise in using the CT@AgNPs as a photocatalyst are the variation of interfering ions and organic species in wastewater, sunlight intensity, and temperature fluctuations, which may affect the adsorption potential of azo dyes on the catalyst's surface. Similarly, the LOD value for detection of Hg^{2+} ions may slightly decrease in the presence of other oxidizing species that can be compensated by developing sequential filtration or selective sedimentation of the sample's interferences before interaction with the CT@AgNPs based sensor. Conclusively, this research might be extended to continuous wastewater treatment by modifying the synthesized catalyst as a self-regenerating filtration membrane. Moreover, the sensor based on CT@AgNPs coated on paper, assisted by smartphone recognition, might be developed for commercial applications.

Data availability

All evaluated data is available in the manuscript. Additional information/data can be provided upon reasonable request.

Author contributions

Z. Khalid & A. B. Siddique: data curation, methodology, investigation, writing – original draft, A. Ali: resources, methodology, validation, writing – review & editing, Y. Zaman & M. F. Sibtain: conceptualization, supervision, project administration, data curation. A. Abbas: conceptualization, writing – review & editing, M. M. Alam: resources, investigation, validation, writing – review & editing, M. S. Alwethaynani: formal analysis, writing – review & editing.

Conflicts of interest

The authors have no known financial or non-financial interests to disclose.

Acknowledgements

The authors extend their appreciation to the Deanship of Research and Graduate Studies at King Khalid University for funding this work through Large Research Project under grant no. RGP2/214/46.

References

1 P. P. Sarma, K. Barman and P. K. Baruah, *Inorg. Chem. Commun.*, 2023, **152**, 110676.

2 N. Mishra, A. Dhwaj, D. Verma and A. Prabhakar, *Anal. Chim. Acta*, 2022, **1205**, 339734.
3 S. D. T. Landa, N. K. R. Bogireddy, I. Kaur, V. Batra and V. Agarwal, *Iscience*, 2022, **25**, 103816.
4 S. Tamilselvan, R. Soniya, R. Vasantharaja, M. Kannan, S. Supriya, B. P. D. Batvari, T. Ramesh and K. Govindaraju, *Environ. Res.*, 2022, **212**, 113585.
5 R. Singh, R. Mehra, A. Walia, S. Gupta, P. Chawla, H. Kumar, A. Thakur, R. Kaushik and N. Kumar, *Int. J. Environ. Anal. Chem.*, 2023, **103**, 1361–1376.
6 A. Numan, A. A. Gill, S. Rafique, M. Guduri, Y. Zhan, B. Maddiboyina, L. Li, S. Singh and N. N. Dang, *J. Hazard. Mater.*, 2021, **409**, 124493.
7 L. Alzahrani, H. A. El-Ghamry, A. L. Saber and G. I. Mohammed, *Arabian J. Chem.*, 2023, **16**, 104418.
8 F. Edition, *WHO Chron.*, 2011, **38**, 104–108.
9 L. Zheng, J. Cui and Y. Deng, *Environ. Sci.:Water Res. Technol.*, 2020, **6**, 2816–2831.
10 Z. Gong, H. T. Chan, Q. Chen and H. Chen, *Nanomaterials*, 2021, **11**, 1792.
11 A. Hyder, J. A. Buledi, M. Nawaz, D. B. Rajpar, Y. Orooji, M. L. Yola, H. Karimi-Maleh, H. Lin and A. R. Solangi, *Environ. Res.*, 2022, **205**, 112475.
12 I. Ivanišević, *Sensors*, 2023, **23**, 3692.
13 D. D. Yılmaz, D. A. Demirezen and H. Mıhçıokur, *Surf. Interfaces*, 2021, **22**, 100840.
14 M. Z. Ishaque, Y. Zaman, Y. Yousaf, M. Shahzad, A. B. Siddique, H. Zaman, S. Ali and N. Ali, *Water, Air, Soil Pollut.*, 2024, **235**, 43.
15 S. Akhtar, S. Shafeeq, A. B. Siddique, F. Y. Sabei, A. Y. Safhi, S. Ullah, A. Abbas, A. Hanbashi, H. Alshahi and A. M. Jali, *J. Power Sources*, 2025, **642**, 236919.
16 F. Sudarman, M. Shiddiq, B. Armynah and D. Tahir, *Int. J. Environ. Sci. Technol.*, 2023, **20**, 9351–9368.
17 E. M. Ahmed, H. Isawi, M. Morsy, M. H. Hemida and H. Moustafa, *Surf. Interfaces*, 2023, **39**, 102980.
18 A. Roy, O. Bulut, S. Some, A. K. Mandal and M. D. Yilmaz, *RSC Adv.*, 2019, **9**, 2673–2702.
19 S. Ying, Z. Guan, P. C. Ofoegbu, P. Clubb, C. Rico, F. He and J. Hong, *Environ. Technol. Innovation*, 2022, **26**, 102336.
20 S. S. Salem and A. Fouda, *Biol. Trace Elem. Res.*, 2021, **199**, 344–370.
21 S. Hazra, A. S. Ray, S. Das, A. Das Gupta and C. H. Rahaman, *Plants*, 2023, **12**, 1495.
22 L. Chabib, H. Hamzah, W. Rahmah, S. F. Sammulia, E. Setyowati and A. Nurfitriani, 2023.
23 C. Hano and B. H. Abbasi, *Biomolecules*, 2021, **12**, 31.
24 M. Kandiah and K. N. Chandrasekaran, *J. Nanotechnol.*, 2021, **2021**, 5512786.
25 Y. Zaman, M. Z. Ishaque, S. Ajmal, M. Shahzad, A. B. Siddique, M. U. Hameed, H. Kanwal, R. J. Ramalingam, M. Selvaraj and G. Yasin, *Inorg. Chem. Commun.*, 2023, **150**, 110523.
26 A. S. Abdelsattar, S. M. Gouda, Y. Y. Hassan, W. M. Farouk, S. Makky, A. Nasr, T. A. Hakim and A. El-Shibiny, *Mater. Lett.*, 2022, **318**, 132184.
27 M. A. Huq, M. Ashrafudoulla, M. M. Rahman, S. R. Balusamy and S. Akter, *Polymers*, 2022, **14**, 742.
28 H. Yousaf, A. Mehmood, K. S. Ahmad and M. Raffi, *Mater. Sci. Eng., C*, 2020, **112**, 110901.
29 A. S. Jain, P. S. Pawar, A. Sarkar, V. Junnuthula and S. Dyawanapelly, *Int. J. Mol. Sci.*, 2021, **22**, 11993.
30 M. Shahzad, M. Z. Ishaque, H. Iqbal, Y. Zaman, A. B. Siddique and H. Zaman, *Phys. Scr.*, 2025, **100**, 035976.
31 N. Assad, M. Naeem-ul-Hassan, M. Ajaz Hussain, A. Abbas, M. Sher, G. Muhammad, Y. Assad and M. Farid-ul-Haq, *Nat. Prod. Res.*, 2023, 1–15.
32 M. Moond, S. Singh, S. Sangwan, P. Devi, A. Beniwal, J. Rani, A. Kumari and S. Rani, *Molecules*, 2023, **28**, 951.
33 S. K. Chandraker, M. K. Ghosh, A. Tiwari, T. K. Ghorai and R. Shukla, *Inorg. Chem. Commun.*, 2022, **146**, 110173.
34 S. R. Khan, S. Jamil, H. Rashid, S. Ali, S. A. Khan and M. R. S. A. Janjua, *Chem. Phys. Lett.*, 2019, **732**, 136662.
35 A. B. Siddique, M. A. Shaheen, A. Abbas, Y. Zaman, A. Ali, M. Naeem-ul-Hassan and J. Iqbal, *J. Environ. Chem. Eng.*, 2024, **12**, 112725.
36 S. Ghaffar, A. Abbas, M. Naeem-ul-Hassan, N. Assad, M. Sher, S. Ullah, H. A. Alhazmi, A. Najmi, K. Zoghebi and M. Al Bratty, *Antioxidants*, 2023, **12**, 1201.
37 V. U. M. Nallal, K. Prabha, I. VethaPotheher, B. Ravindran, A. Baazeem, S. W. Chang, G. A. Otunola and M. Razia, *Saudi J. Biol. Sci.*, 2021, **28**, 3660–3668.
38 E. Abada, A. Mashraqi, Y. Modafer, M. A. Al Abboud and A. El-Shabasy, *Saudi J. Biol. Sci.*, 2024, **31**, 103877.
39 M. Sharifi-Rad, H. S. Elshafie and P. Pohl, *J. Photochem. Photobiol., A*, 2024, **448**, 115318.
40 M. Sundar, G. Rajagopal, A. Nivetha, S. Prabu Kumar and S. Muthukumar, *Separations*, 2024, **11**, 61.
41 Y. Belaiche, A. Khelef, S. E. Laouini, A. Bouafia, M. L. Tedjani and A. Barhoum, *Rev. Rom. Mater.*, 2021, **51**, 342–352.
42 M. M. Aljeldah, M. T. Yassin, A. A.-F. Mostafa and M. A. Aboul-Soud, *Infect. Drug Resist.*, 2023, 125–142.
43 S. Jamil, S. R. Khan, B. Sultana, M. Hashmi, M. Haroon and M. R. S. A. Janjua, *J. Cluster Sci.*, 2018, **29**, 1099–1106.
44 S. Jamil, M. R. S. A. Janjua, S. R. Khan and N. Jahan, *Mater. Res. Express*, 2017, **4**, 015902.
45 J. Wongpreecha, D. Polpanich, T. Suteewong, C. Kaewsaneha and P. Tangboriboonrat, *Carbohydr. Polym.*, 2018, **199**, 641–648.
46 A. B. D. Nandiyanto, R. Zaen and R. Oktiani, *Arabian J. Chem.*, 2020, **13**, 1283–1296.
47 S. Debnath, D. Nath and R. Das, *Phys. B*, 2025, **696**, 416678.
48 M. H. Ali, M. A. K. Azad, K. Khan, M. O. Rahman, U. Chakma and A. Kumer, *ACS omega*, 2023, **8**, 28133–28142.
49 S. R. Khan, S. Jamil, M. R. S. A. Janjua and R. A. Khera, *Mater. Res. Express*, 2017, **4**, 115019.
50 Y. Hao, N. Zhang, J. Luo and X. Liu, *Nano*, 2018, **13**, 1850003.
51 S. Mortazavi-Derazkola, A. Yousefinia, A. Naghizadeh, S. Lashkari and M. Hosseinzadeh, *J. Polym. Environ.*, 2021, 1–9.
52 C. N. Lunardi, A. J. Gomes, F. S. Rocha, J. De Tommaso and G. S. Patience, *Can. J. Chem. Eng.*, 2021, **99**, 627–639.

53 S. Y. Sharaf Zeebaree, O. I. Haji, A. Y. S. Zeebaree, D. A. Hussein and E. H. Hanna, *Catalysts*, 2022, **12**, 1464.
54 N. C. Pomal, K. D. Bhatt, K. M. Modi, A. L. Desai, N. P. Patel, A. Kongor and V. Kolivoška, *J. Fluoresc.*, 2021, **31**, 635–649.
55 S. Ali, X. Chen, W. Shi, G. Huang, L.-m. Yuan, L. Meng, S. Chen, X. Zhonghao and X. Chen, *Crit. Rev. Anal. Chem.*, 2023, **53**, 718–750.
56 F. J. Urbanos, S. Gullace and P. Samorì, *Nanoscale*, 2021, **13**, 19682–19689.
57 J. M. Hudson, G. W. Luther III and Y.-P. Chin, *Environ. Sci. Technol.*, 2022, **56**, 9123–9132.
58 P. Shao, Z. Chang, M. Li, X. Lu, W. Jiang, K. Zhang, X. Luo and L. Yang, *Nat. Commun.*, 2023, **14**, 1365.
59 A. B. Siddique, M. A. Shaheen, A. Abbas, Y. Zaman, M. Z. Ishaque, M. Aslam, K. M. Alsyaad and A. Ali, *J. Mol. Struct.*, 2025, 141566.
60 A. Jabbar, A. Abbas, N. Assad, M. Naeem-ul-Hassan, H. A. Alhazmi, A. Najmi, K. Zoghebi, M. Al Bratty, A. Hanbashi and H. M. Amin, *RSC Adv.*, 2023, **13**, 28666–28675.
61 R. North, *J. Ultrastruct. Res.*, 1963, **9**, 187–197.
62 A. Mai-Prochnow, M. Clauson, J. Hong and A. B. Murphy, *Sci. Rep.*, 2016, **6**, 38610.
63 L. Wang, C. Hu and L. Shao, *Int. J. Nanomed.*, 2017, 1227–1249.
64 C. Kamaraj, C. Ragavendran, K. Manimaran, S. Sarvesh, A. R. M. T. Islam and G. Malafaia, *Sci. Total Environ.*, 2023, **861**, 160575.
65 S. Khan, Z. M. Almarhoon, J. Bakht, Y. N. Mabkhot, A. Rauf and A. A. Shad, *J. Nanomater.*, 2022, **2022**, 3783420.
66 M. F. Alsayed, H. A. Alodaini, I. M. Aziz, R. M. Alshalan, H. Rizwana, F. Alkhelaiwi, S. M. ALSaigh and N. A. Alkubaisi, *Sci. Rep.*, 2024, **14**, 24703.
67 M. E. Mashau, T. Mamagau, K. Foforane, B. Nethathe, M. L. Ramphinwa and F. N. Mudau, *Fermentation*, 2023, **9**, 648.
68 A. B. Siddique, M. A. Shaheen, A. Abbas, Y. Zaman, M. A. Bratty, A. Najmi, A. Hanbashi, M. Mustaqeem, H. A. Alhazmi and Z. ur Rehman, *Heliyon*, 2024, **10**, e40679.
69 B. U. Hijazi, M. Faraj, R. Mhanna and M. H. El-Dakdouki, *Curr. Res. Green Sustainable Chem.*, 2024, **8**, 100408.
70 S. Ajay, J. S. Panicker, K. Manjumol and P. P. Subramanian, *Inorg. Chem. Commun.*, 2022, **144**, 109926.
71 A. B. Siddique, M. A. Shaheen, S. Shafeeq, A. Abbas, Y. Zaman, M. Z. Ishaque and M. Aslam, *Mater. Adv.*, 2025, **6**, 1330–1344.
72 A. B. Siddique, M. A. Shaheen, A. Abbas, Y. Zaman, M. Z. Ishaque, A. Shami, M. Aslam, K. M. Alsyaad and A. Ali, *J. Mol. Struct.*, 2025, **1331**, 141566.
73 M. Ateeb, H. M. Asif, T. Ali, M. M. Baig, M. U. Arif, M. I. Farooq, M. Kaleem and I. Shaukat, *Int. J. Environ. Anal. Chem.*, 2024, **104**, 6928–6946.
74 N. U. Saqib, R. Adnan and I. Shah, *Iran. J. Chem. Chem. Eng.*, 2021, **40**, 1012–1022.